A new methodology for modelling erosion-corrosion regimes on real surfaces: gliding down the galvanic series for a range of metal – corrosion systems.

M.M. Stack*, S.M. Abdelrahman, and B.D. Jana

*Department of Mechanical Engineering

University of Strathclyde

75 Montrose St.,

Glasgow, G1 1XJ

UK

*Corresponding author:

Tel: 00 44 141 548 3754

Fax: 00 44 141 552 5105

E-mail: margaret.stack@strath.ac.uk

1. **Abstract**

Erosion-corrosion of materials in aqueous environments is a complex phenomenon involving a very large number of variables. In such cases, characteristics of the target, particle and the environment

affect the degradation mechanism. Predicting material behaviour may sometimes be a "black art" due to the parameter size which is involved in such processes.

In studies of erosion-corrosion, there have been significant advances in the modelling of such processes in recent years. Various methodologies employed include quasi static modelling, using CFD modeling and erosion-corrosion mapping. In such cases, the output of the various models can differ significantly.

In this work, a methodology combining CFD modelling and erosion-corrosion mapping has been developed to model the erosion-corrosion behaviour of pure metals, which variously passivate and dissolve under a range of simulated conditions. This provides a means of mapping the component undergoing erosion-corrosion and thus is a step change on previous modelling work in this area as it enables superimposition of the erosion-corrosion map on real surfaces. The relative advantages and limitations of this approach are discussed in this paper.

2. Introduction

Particulate erosion-corrosion in aqueous conditions has been the subject of much research in recent years concentrating on a very wide range of materials and conditions. [1-5] Erosion-corrosion is process which is still the subject of much investigation mechanistically. Nonetheless, various modelling approaches have been developed concentrating on many different kinds of output data.

An advance in studying the effects of chemical degradation, caused by corrosion, and mechanical degradation caused by solid particle erosion has been the development of mechanistic maps showing the regime of degradation, the mechanism of wastage and providing a basis for materials selection decisions in a range of conditions [1-5]. Such maps have been developed using predictive models of erosion-

corrosion. However, a limitation of their application to erosion in flowing conditions is that they do not incorporate a parameter relating to fluid flow.

Aqueous fluid flow simulation can be divided into various categories. In the Lagrangian-Eulerian methodology, the Navier-Stokes equations are numerically used to simulate fluid flow processes and the effects of the particles dispersed in the flow are simulated using particle tracking and erosion model techniques. In the Eulerian-Eulearian approach, the fluid and particles are treated essentially as fluids. The first method is thus generally used for dilute multiphase flows where the particle trajectory can be tracked and modeled. For dense flows, where particle–particle interactions may be significant, the two phases can be interpreted and modelled as interacting continuous media [6].

In studies of erosion-corrosion there are no models available which attempt to combine the effects of particle erosion, corrosion and fluid flow with mapping tribo-corrosion methodologies. This has limited the characterization of tribo-corrosion phenomena in real life environments to date.

In this work, various models of solid particle erosion are combined with those for aqueous corrosion. In addition, these models are incorporated in a simulated flowing environment using CFD techniques. The results present a new technique for mapping erosion-corrosion on real pipes, thereby introducing an important step-change in the interpretation of erosion-corrosion mapping techniques to date.

3. Methodology

The initial work involved evaluation of several erosion models against some laboratory erosion results[7]. A methodology was then developed to predict the combined effect of the erosion and corrosion wastage using the model of Sundararajan[8] to predict the erosion rates and a range of

corrosion models to predict the corrosion rates. The total wastage was estimated by combining the erosion rates and the corrosion rates.

The modelling processes thus involved several steps i.e.:

(i) A single elbow- pipe with diameter ratio RD^{-1} of 1.2 with a bore diameter of 0.078 [m] was used for the simulation.

(ii) A standard k-ε model was employed with standard wall function and zero roughness to model the turbulence [9].

(iii) A Lagrangian-Eulerian simulation was used to model the multi-phase flow of the particles trajectories to evaluate the erosion rate using the Discrete Phase Modelling (DPM) method [6]. The DPM method is based on the Lagrangian tracking of every particle using several discritizing methods for tracing the ingested particles (the method used here is Runge-Kutta method).

(iv) A user defined function (UDF) was developed in the above algorithms to evaluate the erosion rate based on the models of Forder et al.[10], Finnie (first model)[11], Neilson-Gilchrist[12], and Sundararajan (second model) [8]. These are outlined in equations 2-5.

(v) A further UDF file was developed to calculate the corrosion and erosion rates at every impact site (according to the original erosion-corrosion mapping methodology generated in 2D [15]).

(vi) For evaluation of the erosion-corrosion rates, Sundararajan's model [8] below was used to calculate the erosion components. The impact angles computed ranged between 7 .5 and 10 ^{o} and this is why this model was used as it accounts for impact angle effects.

The simulation commenced by using a single phase CFD run using FLUENT software and then injecting the particles uniformly at the inlet by using DPM method. A sample of 1655 particles of 10^{-3} [m] diameter was injected with total mass flow rate equal 3.8 [$kg\ s^{-1}$] to represent 22.88% particle concentration which corresponds to particle volume fraction of 0.09.

(The work on 3D maps in this paper was based on earlier studies carried out by Stack and Jana [15], where 2D erosion-corrosion maps for 1mm diameter particle sizes were generated. A particle size of 1 mm was thus chosen to be comparable with results in this earlier study. In ref [15], a value of 25.29% by mass (volume fraction =0.101) was used. This value is marginally above the allowed limit for dilute slurries i.e. 0.1. Thus, a value of 22.88% was chosen which corresponds to a volume fraction of 0.091. This means that the value chosen is within the limit of using Discrete Phase Modelling (DPM) in the FLUENT simulation.)

The walls were chosen as "no slip boundary conditions" and the initial flow velocity was 3 [$m\ s^{-1}$]. The erosion rates were evaluated in terms of volume loss per impact. The total erosion rate over the surface was estimated by calculating the weighted average of all erosion rates on the outer surfaces per unit area i.e. $\dot{W}$ [14]

$$\dot{w}_{av} = \frac{\sum_{node_i} \dot{w}_i A_i}{\sum_{node_i} A_i} \qquad \textbf{(1)}$$

3.1 Erosion models for impact by solid particles

For the various models, the erosion rates $\dot{W}$ are given as follows: (All mathematical terms are given in the list of nomenclature, section 10)

1-) Finnie's erosion model [11]:

$$\dot{W} = C_f \frac{V^2}{P_H \psi k} f(\alpha) \tag{2.a}$$

$$f(\alpha) = \begin{cases} sin(2a) - 4sin^2\alpha & \alpha \le 14.04^o \\ \frac{1}{4} cos^2\alpha & \alpha > 14.04^o \end{cases} \tag{2.b}$$

Finnie recommended a value of 0.1, 2 and 2 for C_f, ψ, and k respectively.

2-) Neilson-Gilchrest model [12]:

$$\dot{W} = \begin{cases} \frac{1}{2}\frac{\left(V^2\cos^2\alpha - V_{tp}^2\right)}{\phi} + \frac{1}{2}\frac{\left(V\sin\alpha - V_K\right)^2}{\varepsilon} & \alpha \le \frac{\pi}{2n} \\ \frac{1}{2}\left[\frac{V^2\cos^2\alpha}{\phi} + \frac{\left(V\sin\alpha - V_K\right)^2}{\varepsilon}\right] & \alpha > \frac{\pi}{2n} \end{cases} \tag{3.a}$$

and $$V_{tp} = V^2\cos^2\alpha\left[\sin(n\alpha) - 1\right] \tag{3.b}$$

3-) Sundararajan's second model [8]:

$$\dot{W}_D = \frac{5.5\times10^{-2}}{\left(T_m - 436\right)^{0.75}} \frac{2^{n_c}\bar{f}_t V^2 \sin^2\alpha\,(1-e^2)}{n_c C_p} \tag{4.a}$$

$$\dot{W}_D = \frac{5.5\times10^{-2}}{\left(T_m - 436\right)^{0.75}} \frac{\left(n_c+1\right)\left(\frac{\mu}{\mu_f}\right)\left(2 - \frac{\mu}{\mu_f}\right)V^2\cos^2\alpha}{\left(1+\lambda\right)2^{2-n_c}\, n_c\, C_p} \tag{4.b}$$

and $\dot{W}_t = \dot{W}_D + \dot{W}_c$ (4.c)

where $\mu_f = \frac{1}{(1+\lambda)(1+e)\tan\alpha}$ (4.d)

$$e = \frac{1.36\, H_s^{0.625}}{E_e^{0.5}\ \rho_p^{0.125} V^{0.25}} \quad (4.e)$$

$$E_e = \frac{E_t E_p}{\left[E_p\left(1-\nu_t^2\right) + E_t\left(1-\nu_p^2\right)\right]} \quad (4.f)$$

4-) Forder's model [10]:

$$\dot{W} = \frac{100 r_p^3}{2\sqrt{29}}\left(\frac{V}{C_k}\right)^{n_f} \sin(2\alpha)\sqrt{\sin\alpha} + \frac{m_p}{2E_e}\left(V\ \sin\alpha - D_k\right)^2 \quad (5.a)$$

$$C_k = \sqrt{3\sigma\frac{R_f^{0.6}}{\rho_p}} \quad (5.b)$$

$$D_k = \frac{\pi^2}{2\sqrt{10}}\left(1.59Y\right)^{2.5}\left(\frac{R_f}{\rho_t}\right)^{0.5}\left[\frac{\left(1-\nu_p^2\right)}{E_t} + \frac{\left(1-\nu_t^2\right)}{E_p}\right]^2 \quad (5.c)$$

3.2 Corrosion and Erosion-Corrosion methodologies

The corrosion rate in the dissolution regime and full details of corrosion reactions anticipated for the pure metals are given elsewhere as generated for the earlier work on 2 dimensional erosion-corrosion maps for the pure metals studied in this paper [15]. The corrosion rate in the dissolution regime is given by:

$$K_c = \frac{RAM\ i_{anet}}{z_m\ Fr} \quad (6.a)$$

where $i_{anet} = i_o \left[\exp\left(\frac{2.303\left(E_{ap} - E_o\right)}{b_a} \right) - \exp\left(\frac{-2.303\left(E_{ap} - E_o\right)}{b_c} \right) \right]$ (6.b)

In the passive region, the corrosion rates estimated for normal impact are given elsewhere [16], based on the work of Tirupataiah et al.[17] for determining a crater diameter for normal impact. To account for the effect of impact angle, we have to modify this approach.

Assuming that the energy involved in the erosion process is the difference between the initial and rebound impact energy and that the erosion process is adiabatic, the energy required to form a crater can be written as:

$$\frac{m_p}{2}\left(V_1^{\,2} - V_2^{\,2}\right) = H_s\, U \tag{7}$$

where m_p is the particle mass, V is particle velocity, H_s is the material hardness, U is the crater volume and the subscripts *1,2* are for the impact and rebound process respectively. Assuming that the surface shear stresses due to oblique impact may be neglected for erosion of brittle materials, Finnie [11] stated that the crater diameter of ring crack d is related to the vertical component of the velocity. Hence, the energy balance in equation (7) is:

$$\frac{m_p}{2}\left(V_1^{\,2}\sin^2\alpha_1 - V_2^{\,2}\sin^2\alpha_2\right) = H_s\, U \tag{8}$$

where α_1 and α_2 are the impact and rebound angles respectively. By definition, the normal impact velocity component is related to the normal rebound velocity component by the coefficient of restitution e, thus and by rearranging:

$$\frac{m_p}{2} V^2 \sin^2 \alpha_1 \left(1 - e^2\right) = H_s \, U \tag{9}$$

Assuming that the particle is a sphere and the crater depth is comparably smaller than the particle diameter, i.e. at low particle velocities, the shape of the crater on the passive film surface can be assumed as part of a sphere and U can be related to the crater diameter D_c by:

$$U = \frac{\pi \, D_c^4}{32 \, d_p} \tag{10}$$

Substitution of equation (10) into (9) gives:

$$D_c = 1.5023 \left[\frac{m_p \, d_p \left(1 - e^2\right)}{H_s} \right]^{0.25} \left(V \, \sin \alpha_1\right)^{0.5} \tag{11}$$

The crater depth d is related to crater diameter using the same assumption above by:

$$d = \frac{D_c^2}{4 \, d_p} \tag{12}$$

From [15], the mass of passive film removed per impact is given as:

$$M_t = \pi \, k_2 \, d_p \, d \, h \, \rho_f \tag{13}$$

Substituting equation (11) into (12) and apply to (13):

$$M_t = \pi k_2 \, h \, \rho_f d_p^2 \left[\frac{\rho_p \left(1 - e^2\right)}{6 H_s} \right]^{0.5} \left(V \, \sin \alpha_1\right) \tag{14}$$

The unit given for the erosion model by equation (14) is [*kg impact*$^{-1}$]. To convert to K_e [*kg m*$^{-2}$ *s*$^{-1}$], the erosion rate, equation (14) can be multiplied by particle impact frequency as outlined in [15]. This can be varied according to the application under investigation. For example, if the flow is homogeneous (constant particle concentration) then particle impact frequency may be given as:

$$I_p = \frac{cV \sin\alpha}{m_p} \qquad (15)$$

and c is the particle concentration by mass [$kg\ m^{-3}$].

For evaluation of properties of the pure metals and their passive films, the mechanical properties for Fe, Ni, Cu and Al are given below, in table (1). The constant k_2 is defined as the mass ratio between the metal and its oxide created during the corrosion reaction multiplied by the number of moles of metal involved in the reaction [15].

The thickness of the passive layer h can be assumed to be varied with the potential difference and may be given from [15]:

$$h = h_o + 3\times10^{-9}\left(E_{ap} - E_{pas}\right) \qquad (16)$$

and: $h_o = 1\times10^{-9}\ [m]$

All corrosion rates must be calculated in [$gm\ cm^{-2}\ s^{-1}$]. The erosion rates from Sundararajan's model [8] must be converted from [$kg_{target}\ kg_{particle}^{-1}$] accordingly as indicated above.

Equation (14) is a simple expression for estimating the erosion rates for the passive film on a substrate. It is valid only for the impact of passive film formed during the erosion-corrosion process where the erosion footprint (i.e. the deformed surface) has a ring shape approximately (this is also assumed at oblique impact angles). The equation is useful for CFD applications in which erosion occurs at a range of impact angles. Should the particle fully penetrate the passive film and erode the substrate, another approach is considered i.e. the use of a model for erosion of ductile materials [8].

The calculation of K_{ec}, the total erosion-corrosion rate is outlined below.

3.3 Erosion-corrosion mapping boundaries

The regime boundaries are defined in terms of the ratio K_c/K_e. Therefore, by combining and rearranging the above expression for K_c, and K_e, the boundaries for the erosion-corrosion regime maps at a given applied potential can be determined as [15]:

$$\frac{K_c}{K_e} < 0.1 \qquad \text{(Erosion dominated)} \qquad (17)$$

$$0.1 \le \frac{K_c}{K_e} < 1 \qquad \text{(Erosion-Corrosion dominated)} \qquad (18)$$

$$1 \le \frac{K_c}{K_e} < 10 \qquad \text{(Corrosion-Erosion dominated)} \qquad (19)$$

$$\frac{K_c}{K_e} \ge 10 \qquad \text{(Corrosion- dominated)} \qquad (20)$$

where in the dissolution region, K_c can be determined from equation (6-a,b). In the passive region, the corrosion rate is equal to the additive effect of the erosion on corrosion (i.e. erosion controlled corrosion or simply repassivation) which can be given directly from equation (14). (The Pourbaix diagrams, Fig 1, indicate whether corrosion process involved in the erosion-corrosion interaction will be erosion-dissolution or erosion-passivation as a function of the pH and potential The ratios of the corrosion to the erosion contributions above identify which process dominates ie. If the corrosion rate is 10 times the erosion rate then the surface is corrosion dominated and if the Pourbaix diagram, Fig. 1, indicates that dissolution can only take place, then the process is dissolution dominated).

In order to present the erosion-corrosion regime on the pipe surface, the K_c/K_e ratios at each node in the pipe surface are evaluated and contour plots are generated to generate transition boundaries of the

erosion-corrosion regimes above.

The total wastage in the active and passive regimes can be given by:

$$K_{ec} = K_c + K_e \tag{21}$$

The transition boundaries for the wastage maps:

$$K_{ec} < 1 \quad [mm\ year^{-1}] \quad \text{(low wastage)} \tag{22}$$

$$1 \le K_{ec} < 10 \quad [mm\ year^{-1}] \quad \text{(medium wastage)} \tag{23}$$

$$K_{ec} \ge 10 \quad [mm\ year^{-1}] \quad \text{(high wastage)} \tag{24}$$

Plots of these regimes at each node in the pipe were generated for the wastage maps below. The erosion-corrosion maps constructed in this work are based on the pure metals data, electrochemical reactions, and pH values used in [15] and are considered an extension from 2D to 3D mappings taking into consideration the effect of the fluid flow properties on the erosion-corrosion mappings, assuming potential controlled corrosion.

4. Results

To clarify the dissolution and passive regions of influence for every pure material selected in this study, Fig. 1 illustrates the Pourbaix diagrams for Fe, Ni, Cu, and Al respectively. These diagrams are the basis for constructing the erosion-corrosion maps below as they determine the corrosion regimes which predominate for each of the pure metals (i.e. dissolution, passivation and immunity). As is shown from the figures, significant differences in the stability regimes are observed for the pure metals as a function of pH and potential which, in the context of the erosion-corrosion maps, will be discussed further below.

4. 1 Erosion model predictions

Fig. 2 indicates the various predictions of the erosion models and it can be seen that there are similarities between the erosion rates calculated and evaluated in earlier work [7] when the values in the earlier study were used and hence this was a useful calibration exercise. The predictions on real surfaces are indicated in Fig. 3 where the highest erosion rates were observed at the bend in the pipe. Analysis of the impact frequency; Fig. 4 and the impact velocity profile. Fig. 5 indicates the area around the bend experienced the highest impact frequency and velocities.

4. 2 Effect of pH on the erosion-corrosion regime mapping for pure metals

The erosion-corrosion mapping results Fig. 6 (a-d) show the change in erosion-corrosion regimes for the various pure metals at pH 5 and -0.6 V (SCE). It is clear that there were a number of erosion-corrosion regimes operating on the component, under nominally the same initial simulation conditions. Here, it was shown that there were significant differences between the regimes of erosion-corrosion behaviour observed, with dissolution and dissolution-erosion being dominant for Fe, Fig. 6(a), a transition to erosion-dominated behaviour for Ni and Cu, Fig. 6(b-c) and to erosion-passivation for Al, Fig. 6 (d). At pH 7, Fig. 7, as was observed at pH 5, Fig. 6, only Fe, Fig. 7(a), was affected by dissolution. All the other metals were in the erosion-dominated or in the case of Al, Fig. 7(d), passivation affected regimes. At pH 9, Fig 8, there was a transition to erosion-passivation and erosion-dominated behaviour for the Fe, Fig. 8(a) which contrasted with the behaviour at lower pH values; Fig. 6(a) and 7 (a); in which dissolution affected the process. For the Ni and Cu, the erosion-corrosion processes were again characterized by erosion-dominated behaviour, Fig. 8 (b-c). For Al, Fig. 8(d) there was a transition to a

new corrosion affected regime, dissolution dominated behaviour, which contrasted with the passivation dominated processes observed at the lower pH values, Fig. 6(d), 7(d).

4. 3 Effect of particle size and applied potential on erosion-corrosion mapping of Fe

For the effect of particle size on Fe at pH 9 and -0.6 V (SCE), Fig. 9, increases in particle size by a factor of three, Fig. 9(a-c) changed the erosion-corrosion processes from passivation dominated and passivation-erosion dominated behaviour to a situation where erosion-passivation was the dominant degradation process, with the extent of this regime prevailing being greater at the higher potentials, Fig. 9(b-c). Increases in applied potential, however, Fig. 10 for Fe at pH 7 showed various significant transitions from mainly erosion dominated behaviour at -0.75 V(SCE), Fig. 8(a) to dissolution and mainly erosion-passivation dominated behaviour as the potential was increased from t -0.5 to -0.25 V, Figs. 10(b-c).

4. 4 Comparison between erosion-corrosion wastage maps at the various pH values

The results on erosion-corrosion wastage maps, Figs. 11-13, indicate very significant differences for the pure metals at the various pHs. As in the case for the results above, a number of wastage regimes predominated on the component. At pH 5, the highest wastage was observed for the Fe, Fig. 11 (a), with the wastage decreasing for Ni and Cu, Fig. 11(b-c). The high wastage regime had a greater presence for Al, Fig. 11(d) than for the latter metals, Fig. 11 (b-c). As the pH was increased to 7, the wastage profiles were similar for all metals, Fig. 12 (a-d) as had been the case at pH 5, Fig. 11. However, at pH 9, there

was a change in the behaviour, Fig. 13(a-d) with the high wastage regime predominant for the Al, Fig. 13 (d), to a greater extent than for the other metals.

5. Discussion

The results indicate that it is possible to simulate the erosion-corrosion mapping process on real components using such an approach. It is shown that a number of mechanistic regimes are possible, under nominally the same initial tribo-corrosion conditions, Figs. 6-13, and that this may be in part related to the difference in impact frequencies and velocities, Figs. 4-5 observed on the component. This means that designing materials and processes for optimum erosion-corrosion resistance is a complex problem with more than one erosion-corrosion regime possible on a single component.

It is interesting that, as in the two dimensional simulations for erosion-corrosion of pure metals,[15] significant differences are found in the three-dimensional simulation between the regimes dominating for the metals, with Cu and Ni being more immune and less likely to be dominated by corrosion than Fe and Al, under the window of conditions employed in the model, Figs. 6-8. However, it should be emphasized that if the conditions differ the results will change significantly. Moreover, it is important to note that various metals will exhibit different erosion-corrosion behaviour and because of the changes of velocity and particle frequency of impact over the component, Fig. 4 and 5, a variety of erosion-corrosion regimes are experienced on the surface of the component.

It is clear that a significant area of the component modelled will not experience any erosion or impact of flowing particles, Figs. 6-13. In practice, the un-eroded surfaces may experience corrosion through dissolution or passivation. Moreover, the corrosion process may be controlled by the flow parameters

(flow controlled corrosion) such as fluid temperature and the oxygen concentration in the bulk flow [18,19]. The effect of these parameters will be addressed in further work.

The transition from passivation to dissolution dominated behaviour for Al, is illustrated in Figs. 6(d), 8(d). Here, at higher pH values, the Al dissolves, in contrast to that which occurs for the other pure metals at such pHs, Fig. 8. This is a characteristic of Al which makes it unsuitable for use at such pH values.

Increases in particle size by a factor of three, Fig. 9, for the Fe, not surprisingly, reduces the passivation affected regimes on the component. The increase in erosion footprint results from the higher impact energy involved in the process. The three dimensional results highlight the important influence that particle size has on the erosion-corrosion regime.

The effect of changing applied potential in the positive direction, i.e. from -0.75 to -0.25 V(SCE), Fig. 10(a-c), has a very significant effect on the erosion-corrosion degradation mode for the Fe. Here, the regime is changed from dissolution to predominately passivation affected behaviour over the component. This illustrates the important of electrochemical potential on the stability of the corrosion regime as identified by the Pourbaix diagrams for the various pure metals and their influence on the erosion-corrosion two-dimensional maps[15].

The wastage regime maps for the pure metals, Figs. 11-13, show very little differences between the pure metals at pH 5 and 7, at -0.6 V (SCE) which is surprising. However, at the higher pH values, the

wastage is significantly greater for the Al, Fig. 13(d) than at lower pH values, possibly due to the high dissolution rate of this material.

A limitation of the model developed to date is that it assumes no interaction between erosion and corrosion i.e. no synergy or antagonism during the processes. However, the reasons for such effects are not well understood and can be material specific [5, 19-20]. This is why the initial work on mapping the component for the materials above has made such assumptions. Further work will be to incorporate such effects in the model, particularly in the case where they can be directly related to material properties i.e. for the erosion-corrosion of composites both in bulk and in coating form [5].

It is acknowledged that in situations where re-passsivation cannot take place due to a very short duration between impacts , a transition to erosion affected dissolution behavior may occur as identified in other tribo-corrosion studies in aqueous environments [22]. This is a potentially complex situation which has not been considered to date in the above approach. Further work will be to consider the more complex interactions in erosion-corrosion as discussed above.

Hence, the model developed provides a new tool for representing the transitions between erosion-corrosion regimes on real surfaces. The results indicate the variety of regimes possible over one single component. Further work will be to investigate a range of other variables in the model, such as temperature and oxygen concentration, in addition to the above issues together with identifying how materials and process parameters may be optimized for erosion-corrosion resistance using such an approach.

6. Conclusions

(i) CFD methods which involve fluid dynamics and multiphase flow parameters have been used to model the erosion-corrosion behaviour of a range of metal-corrosion systems.

(ii) The results indicate that it is possible to identify erosion-corrosion mechanistic regimes on real components using the analysis and show the wide range of regimes possible under nominally similar fluid flow conditions.

(iii) The effect of erosion and corrosion parameters such as particle size and applied potential show significant differences on the three dimensional erosion-corrosion regimes indicating the important effect of erosion-corrosion variables on the stability of such regimes observed on real life components.

7. References

1 Stack M.M., Stott F.H.: An approach to modeling erosion-corrosion of alloys using erosion-corrosion maps. Corrosion Science 1993; 35:1027-1034.

2 Stack M.M., Lekatos S., Stott F.H.: Erosion-corrosion regimes: Number, nomenclature and justification? Tribology International 1995; 28:445-451.

3 Stack M.M., Corlett N., Zhou S.: Construction of erosion-corrosion maps for erosion in aqueous slurries. Materials Science and Technology 1996; 12:662-672.

4 Stack M.M.: Some issues relating to the construction of materials selection maps for resistance to elevated temperature erosion. Tribology International 1997; 30:435-444.

5 Stack M.M., Abd El-Badia T.M.: Some comments on mapping the combined effects of slurry concentration, impact velocity and electrochemical potential on the erosion-corrosion of WC/Co-Cr coatings. Wear 2008; 264:826-837.

6 Kolev N.I.: Multiphase flow dynamics 1: Fundamentals, 2nd edition. New York, Springer Berlin Heidelberg, 2004.

7 Wood R.J.K., Jones T.F., Ganeshalingam J., Miles N.J.: Comparison of predicted and experimental erosion estimates in slurry ducts. Wear 2004; 256:937-947.

8 Sundararajan G.: A comprehensive model for the solid particle erosion of ductile materials. Wear 1991; 149:111-127.

9 Launder B.E.: Lectures in mathematical models of turbulence. London, Academic Press, 1972.

10 Forder A., Thew M., Harrison D.: A numerical investigation of solid particle erosion experienced within oilfield control valves. Wear 1998; 216:184-193.

11 Finnie I: Erosion of surfaces by solid particles. Wear 1960; 3:87-103.

12 Neilson J.H., Gilchrist A.: Erosion by a stream of solid particles. Wear 1968; 11:111-143.

13 Pourbaix M.: Atlas of electrochemical equilibria in aqueous solutions. Oxford, New York, Pergamon Press, 1966.

14 FLUENT Inc.: Fluent user's guide, version 6.3. Lebanon, NH, USA, 2006,

15 Stack M.M., Jana B.D.: Modelling particulate erosion-corrosion in aqueous slurries: Some views on the construction of erosion-corrosion maps for a range of pure metals. Wear 2004; 256:986-1004.

16 Jana B.D., Stack M.M.: Modelling impact angle effects on erosion-corrosion of pure metals: Construction of materials performance maps. Wear 2005; 259:243-255.

17 Tirupataiah Y., Venkataraman B., Sundararajan G.: The nature of the elastic rebound of a hard ball impacting on ductile, metallic target materials. Materials Science and Engineering A-Structural Materials Properties Microstructure and Processing 1990; 124:133-140.

18 Stott F.H., Jordan M.P., Lekatos S., Stack M.M., Wood G.C.: The erosion-corrosion of alloys under oxidizing-sulfidizing conditions at high-temperature. Wear 1995; 186:291-298.

19 Stack M.M., Corlett N., Turgoose S.: Some thoughts on modelling the effects of oxygen and particle concentration on the erosion-corrosion of steels in aqueous slurries. Wear 2003; 255:225-236.

20. Stack M.M., Antonov M. and Hussainova I.: some views on the the erosion-corrosion response of bulk chromium carbide cermets. J Phys D: Applied Physics, 2006, 39:3165-3174.

21. Stack M.M. and Abd El-Badia T.M., Mapping erosion-corrosion of WC/Co-Cr based composite coatings: particle velocity and applied potential effects. Surface and Coatings Technology, 2006, 201, 3-4, 1335-1347.

22. Stack M. M. and Chi K., Mapping sliding wear of steels in aqueous conditions. Wear 2003; 255: 456-465.

8. List of Figures:

Figure 13: Erosion-corrosion wastage maps for the outer surface of elbow-pipe at pH=9, E_{ap} =-0.6 V[SCE], particle size=1000 [μm] and concentration =22.88% (vf= 0.1) for: (a) Fe (b) Ni (c) Cu (d) Al.

9. List of tables:

Table 1: Properties for pure metals selected and their passive films.

10. Nomenclature:

Latin letters:

A_i	Area of the surface cell.		[m^2]
b_a	Anode Tafel slope		[V $decade^{-1}$]
b_c	Cathode Tafel slope		[V $decade^{-1}$]
C_f	Non-dimensional constant (Finnie)	0.5	
C_k	Cutting characteristic velocity (Forder)		[m s^{-1}]
C_p	Specific heat capacity		[J Kg^{-1} K^{-1}]
c	Particle concentration		[g cm^{-3}]
D, D_c	Diameter of the pipe roundness, Crater diameter		[m]
D_k	Deformation characteristic velocity (Forder)		[m s^{-1}]
d	Pipe diameter, crater depth		[m]
E	Applied potential, relative to saturated calomel electrode, Modulus of elasticity of the material.		V[SCE], [Pa]

E_e	Reduced Young's modulus of elasticity (modulus of collision)		[Pa]
e	Coefficient of restitution		
Fr	Faraday's constant	96485	[C mol^{-1}]
$f(\alpha)$	Function depends on the impact angle		
f_t	Numerical constant	0.025	
H	Hardness		[Pa]
h	Thickness of the oxide layer		[m]
h_o	Initial thickness of the oxide layer		[m]
I_p	Impact frequency		[imp cm^{-2} s^{-1}]
i_{anet}	Net anodic current density		[A m^{-2}]
i_o	Exchange current density		[A m^{-2}]
K_c	Corrosion rate		[kg m^{-2} s^{-1}]
K_{ec}	Total wastage rate		[kg m^{-2} s^{-1}]
K_e	Erosion rate		[kg m^{-2} s^{-1}]
k	Ratio of vertical to horizontal forces (Finnie)	2	
k_2	metal to its oxide molecular mass ratio [8]		
M_t	Total erosion rate by single impact particle		[Kg $impact^{-1}$]
m_p	mass of impacting particle		[Kg]
n	Empirical constant (Neilson-Gilchrist)		
n_f	Velocity ratio exponent (Forder)	2.54	
n_c	Strain hardening coefficient	0.3	
P_H	Eroding surface flow stress related to hardness (Finnie)		[Pa]
RAM	Relative atomic mass		

R_f	Particle roundness factor (Forder)	0.5	
r_p	radius of impacting particle		[m]
T_m	Melting temperature point of the metal		[K]
U	Crater volume		[m^3]
V	Velocity,		[m s^{-1}]
vf	Volume fraction of particles		
W	Erosion rates		[m^3 $impact^{-1}$]
W_C	Erosion by cutting		[kg kg^{-1}]
W_D	Erosion by deformation		[kg kg^{-1}]
W_t	Total Erosion (Sundararajan)		[kg kg^{-1}]
w_{av}	Area weighted average wastage of metal		[kg m^{-2} s^{-1}]
w_i	Wastage of metal at centre node on the eroded surface cell		[kg m^{-2} s^{-1}]
Y	Yield stress of the target material(Forder)		[Pa]
z_m	number of electrons		

Greek letters:

α	impact angle		[deg]
ε	Deformation wear factor (Neilson-Gilchrist)		
λ	Particle shape factor	0.0	
μ	Frictional coefficient	0.1	
μ_f	Critical friction coefficient (Sundararajan)		
ν	Poisson's ratio		
π	Pi ratio	3.1416	

ρ	Density		[Kg m^{-3}]
ρ_p	Density of the particle	2650	[Kg m^{-3}]
Φ	Cutting wear factor (Neilson-Gilchrist)		
Ψ	Ratio of depth of contact to depth of cut (Finnie)	2	

Subscripts:

p	Particle
pas	passivation
s	Substrate
o	initial, Reversible equilibrium potential
f	Friction, oxide film
t	total, target
i	Node
c	Corrosion, crater
e	Erosion, reduced elasticity
m	Melting
1	Impact
2	Rebound
ap	Applied potential
av	Average
ce	Total wastage due to erosion and corrosion
K	Threshold, deformation(N-G)
tp	threshold, cutting (N-G)

11. List of Figures:

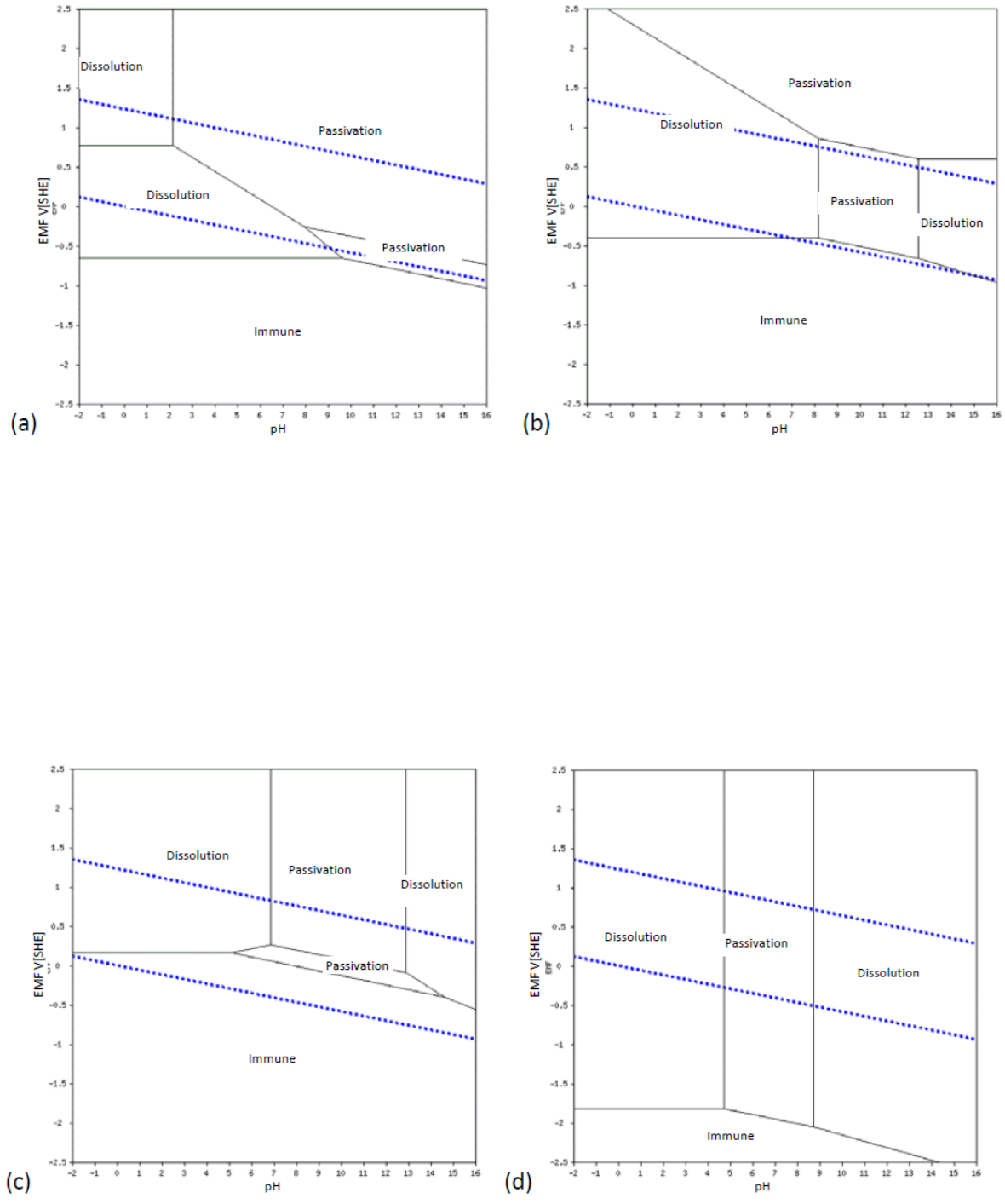

Figure 1: Pourbaix diagrams for: (a) Fe (b) Ni (c) Cu (d) Al. [13]

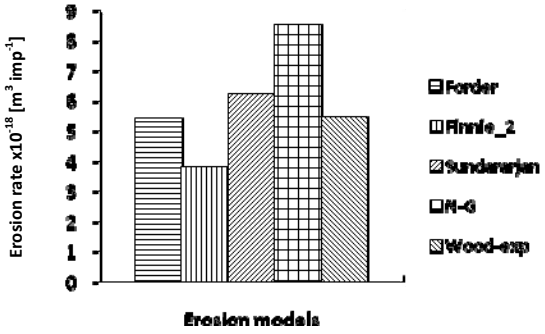

Figure 2: Prediction of erosion models [10], [11], [8], [12] and comparison with experimental results[7].

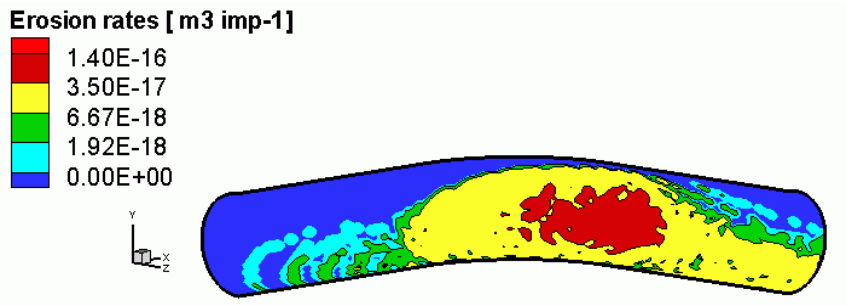

Figure 3: Erosion rates contours on the outer surface predicted by (DPM) Discrete Particle Method

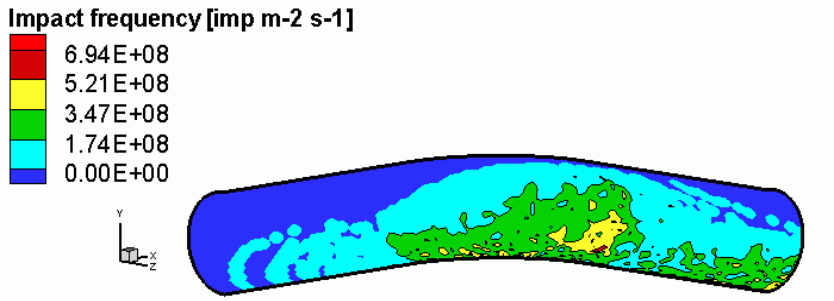

Figure 4: Impact frequency by (DPM) Discrete Particle Method

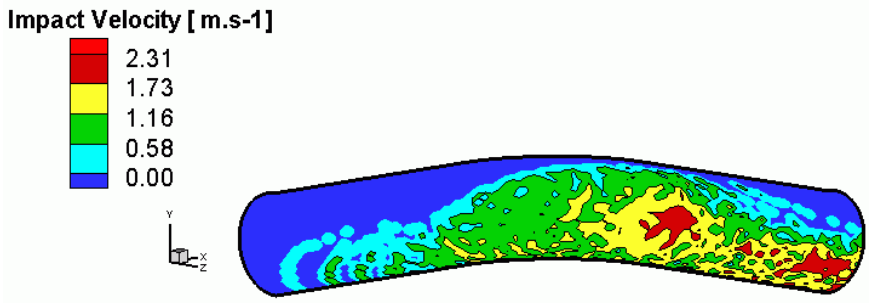

Figure 5: Impact velocity profile on the surface of the elbow-pipe

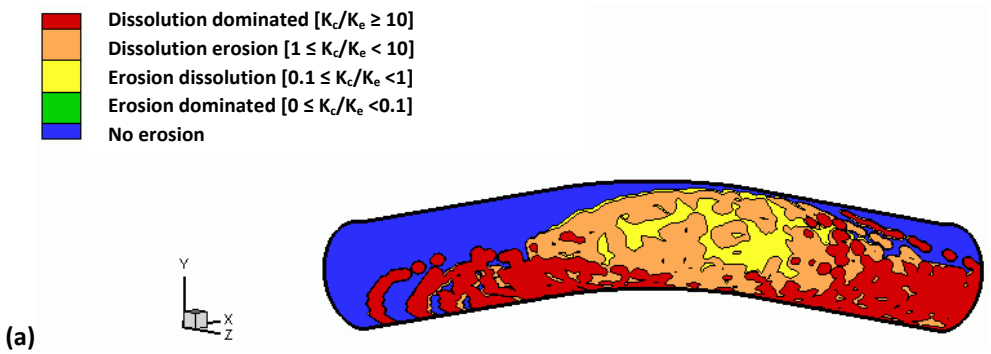

(a)

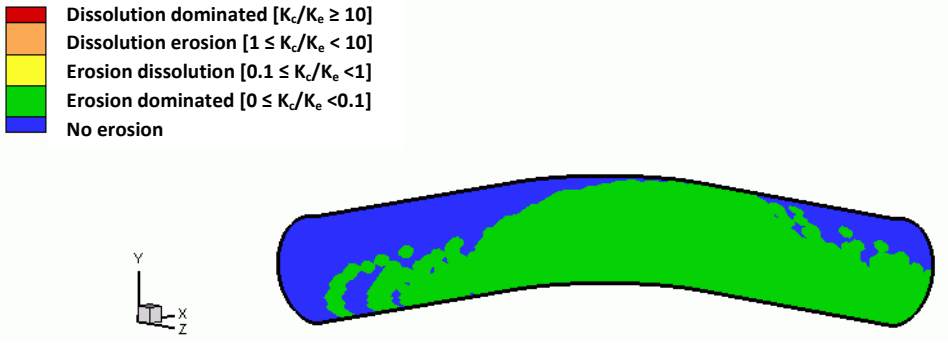

(b)

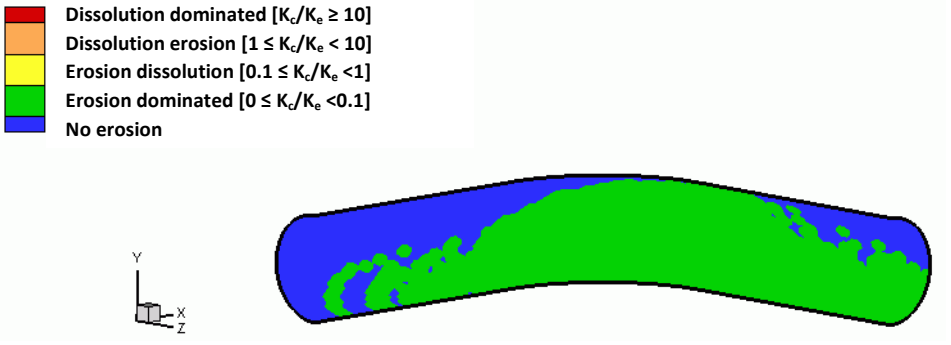

(c)

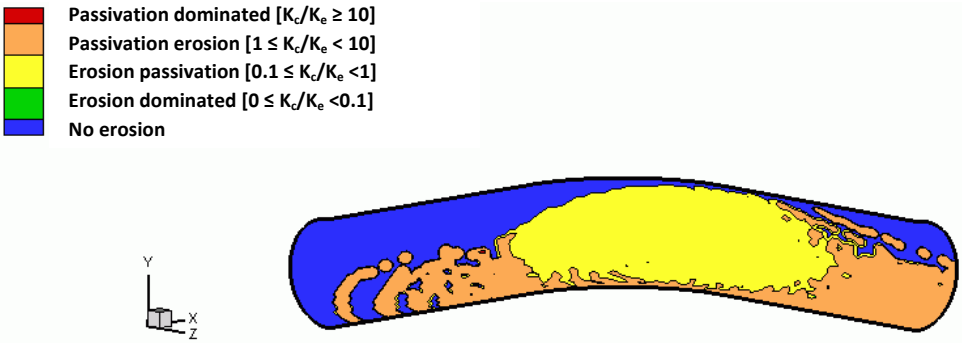

(d)

Figure 6: Erosion-corrosion maps for the outer surface of elbow-pipe at pH=5, E_{AP}=-0.6 V[SCE], particle size=1000 [µm] and concentration =22.88% (vf= 0.1) for: (a) Fe. (b) Ni. (c) Cu. (d) Al.

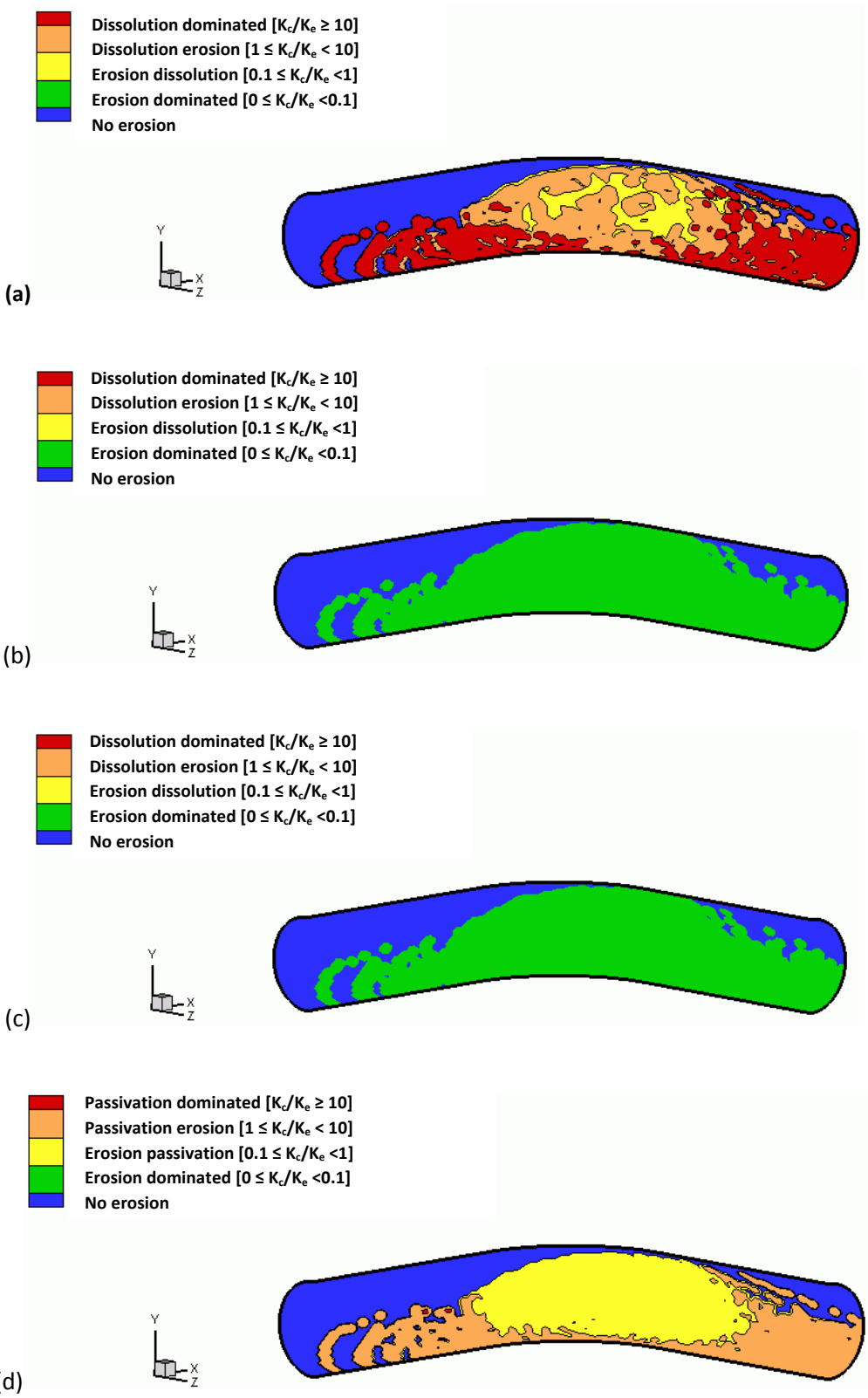

Figure 7: Erosion-corrosion maps for the outer surface of elbow-pipe at pH=7, E_{AP}=-0.6 V[SCE], particle size=1000 [µm] and concentration =22.88% (vf= 0.1) for: (a) Fe. (b) Ni. (c) Cu. (d) Al.

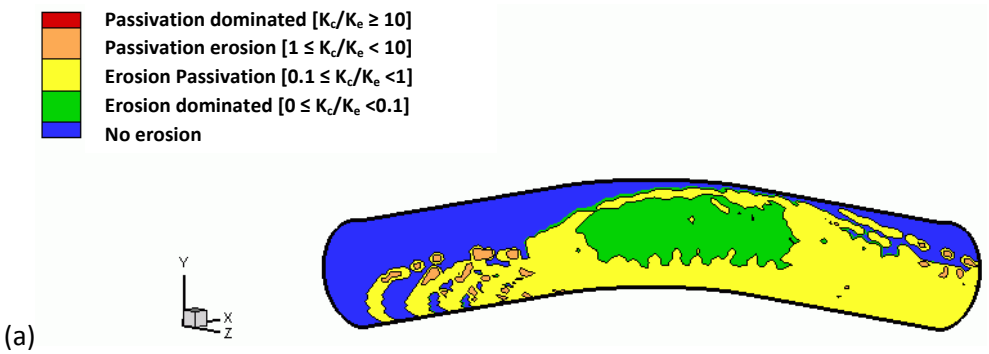

(a)

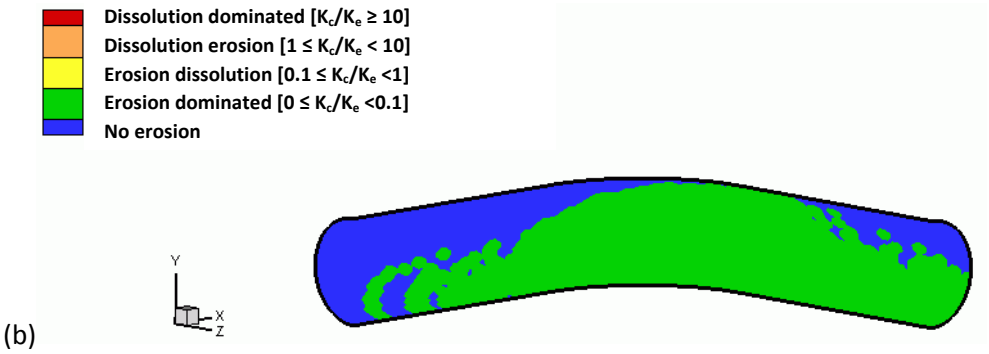

(b)

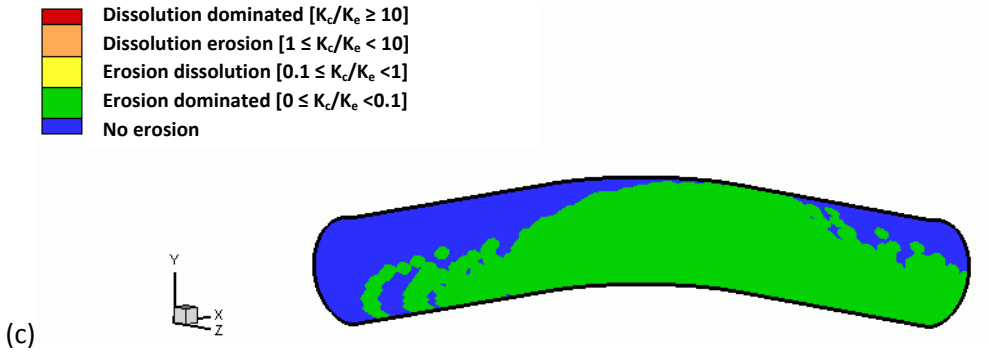

(c)

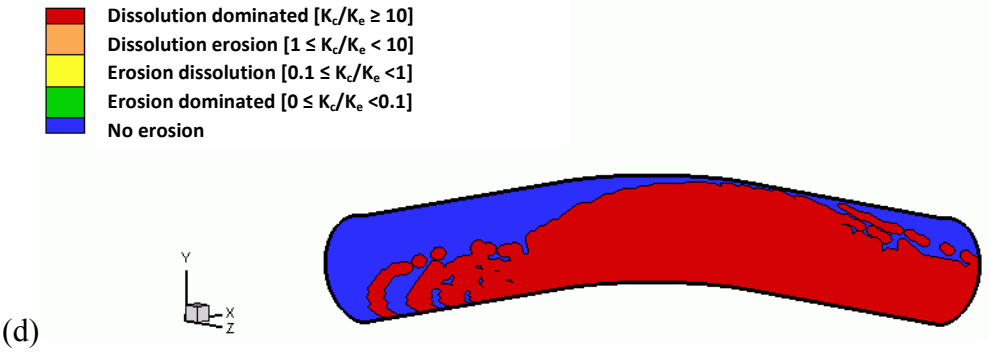

(d)

Figure 8: Erosion-corrosion maps for the outer surface of elbow-pipe at pH=9, E_{AP} =-0.6 V[SCE], particle size=1000 [µm] and concentration =22.88% (vf= 0.1) for: (a) Fe. (b) Ni. (c) Cu. (d) Al.

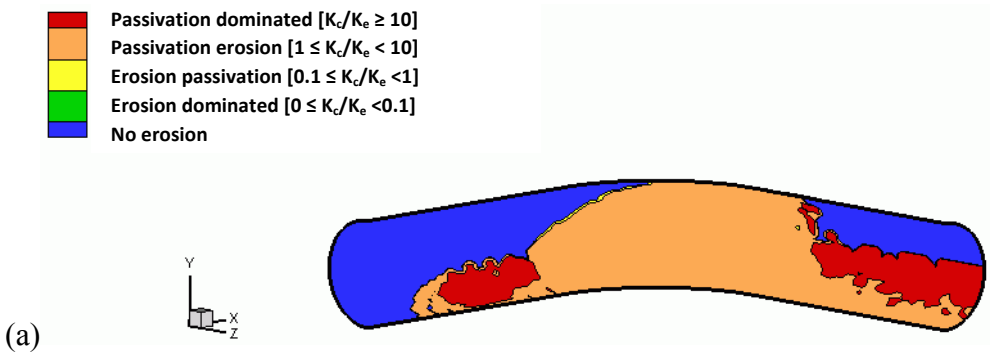

(a)

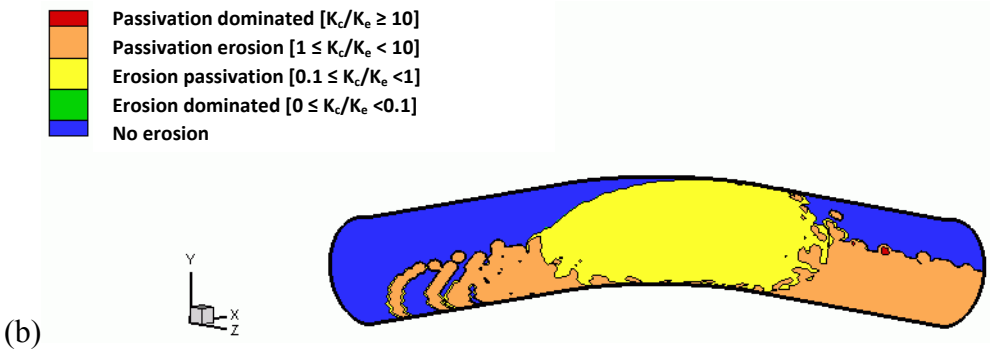

(b)

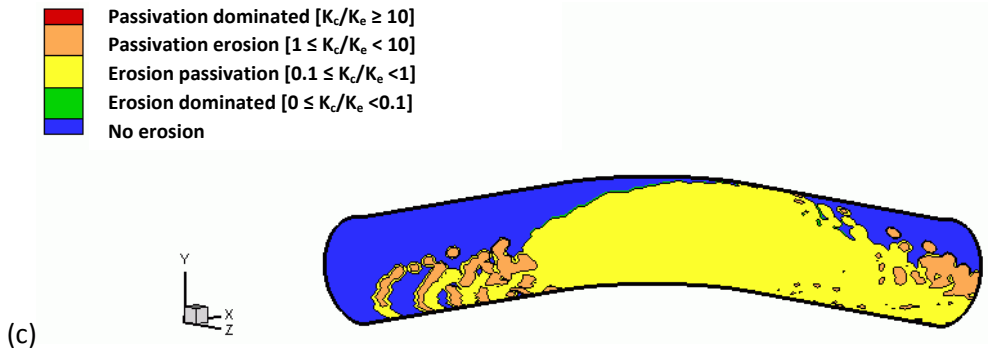

(c)

Figure 9: Erosion-corrosion maps for the outer surface of (Fe) elbow-pipe at pH=9, E_{AP} =-0.6 V[SCE] and concentration=22.88% (vf= 0.1) for particle size: (a) 250 [µm]. (b) 500 [µm]. (c) 750 [µm].

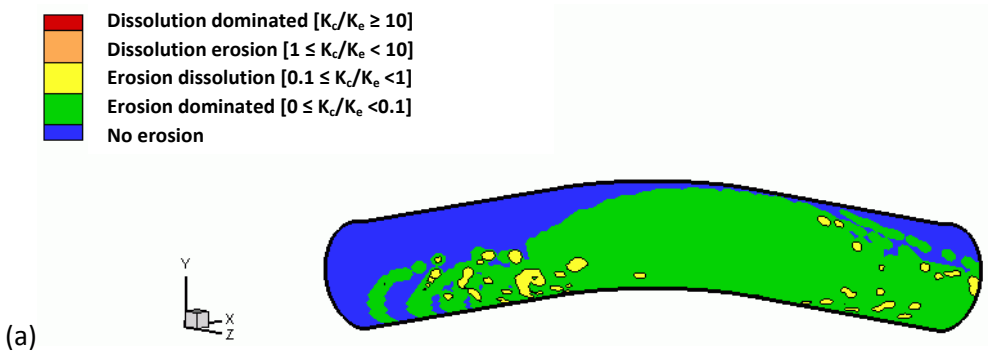

(a)

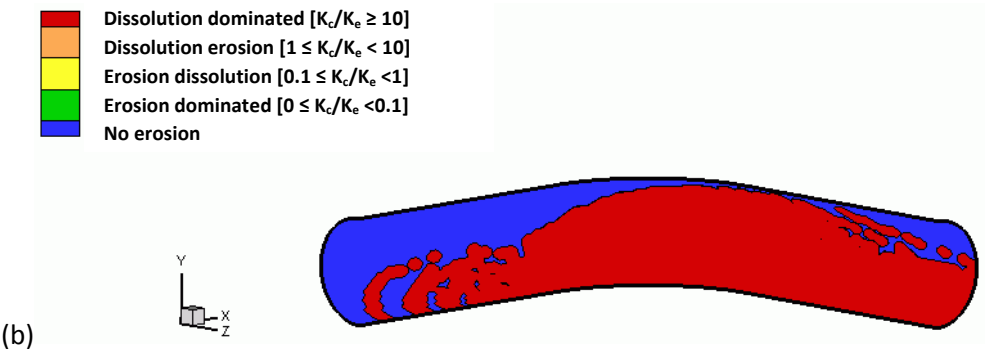

(b)

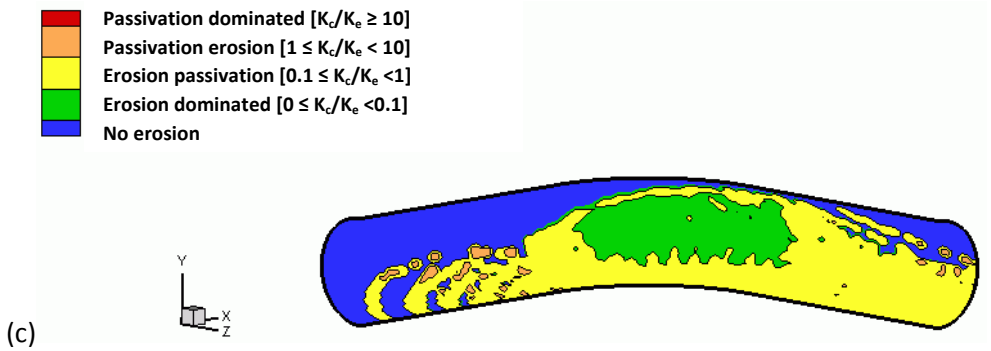

(c)

Figure 10: Erosion-corrosion maps for the outer surface of (Fe) elbow-pipe at pH=7, particle size=1000 [µm] and concentration =22.88% (vf= 0.1) for E_{AP}: (a) -0.75 (b) -0.5 (c) -0.25 V[SCE].

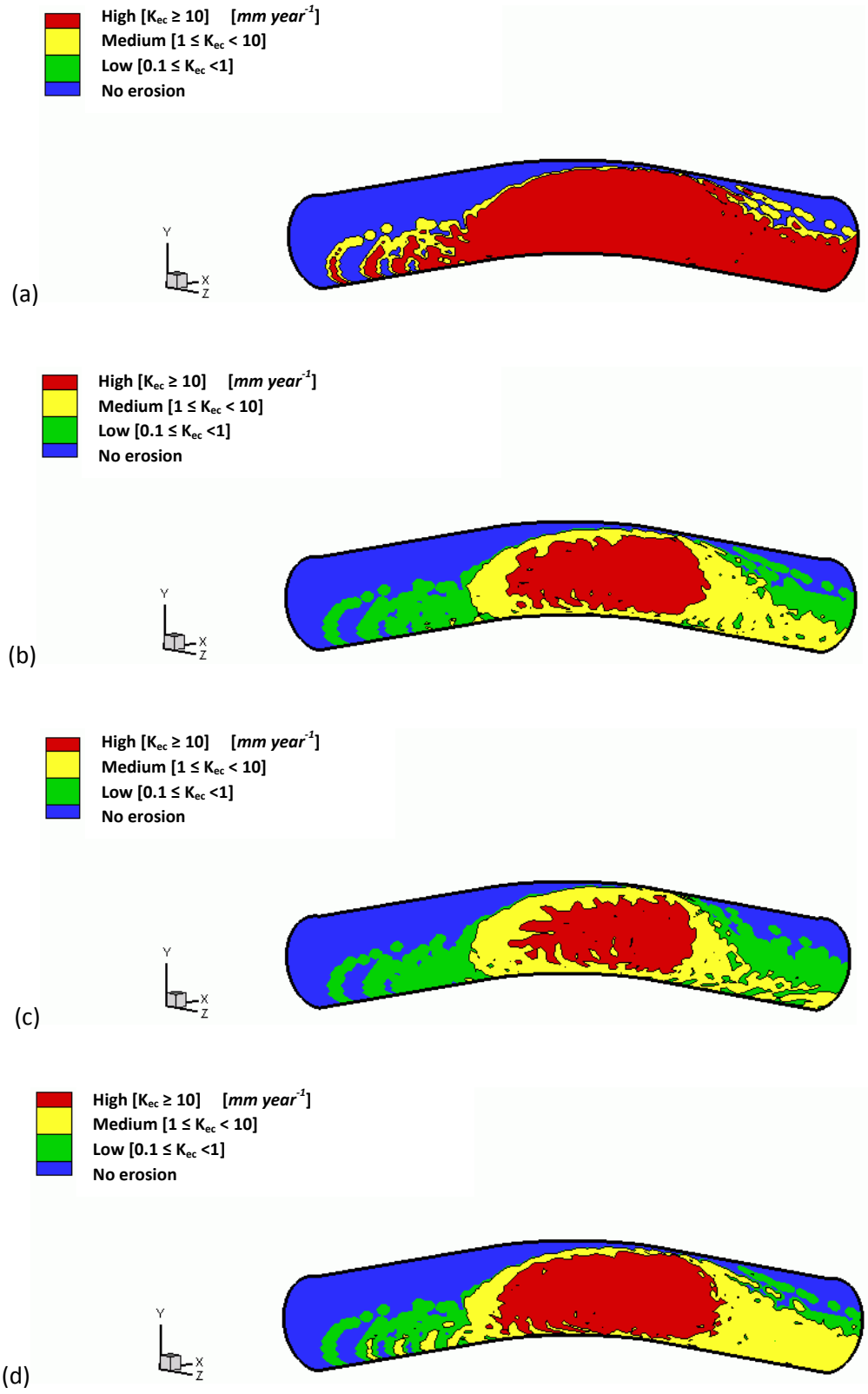

Figure 2: Erosion-corrosion wastage maps for the outer surface of elbow-pipe at pH=5, E_{AP} =-0.6 V[SCE], particle size=1000 [μm] and concentration =22.88% (vf= 0.1) for: (a) Fe. (b) Ni. (c) Cu. (d) Al.

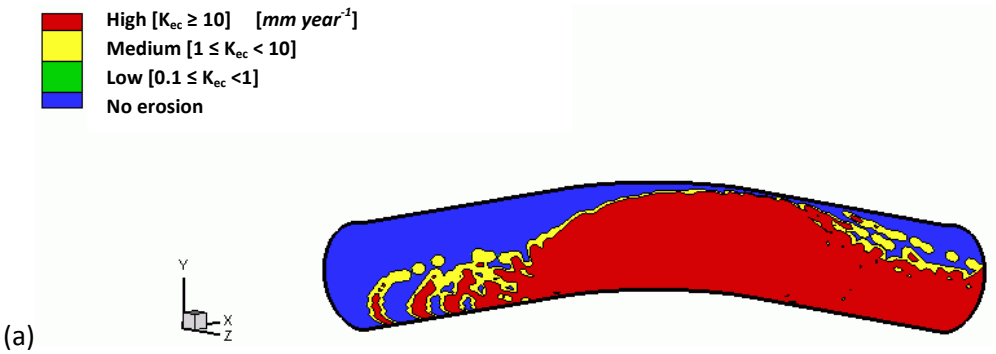

(a)

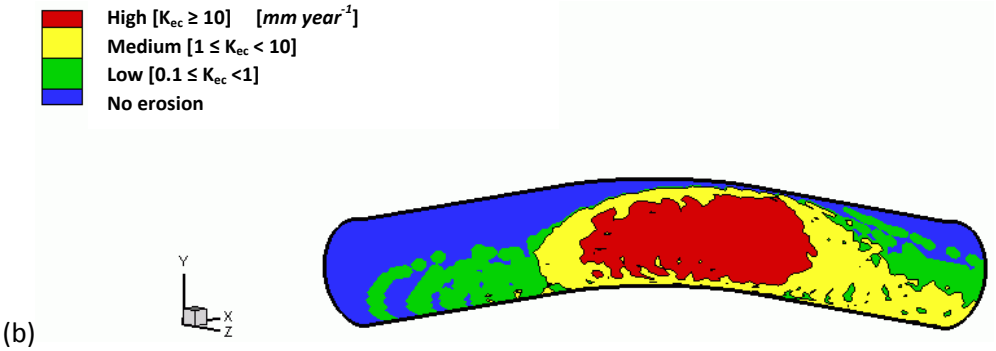

(b)

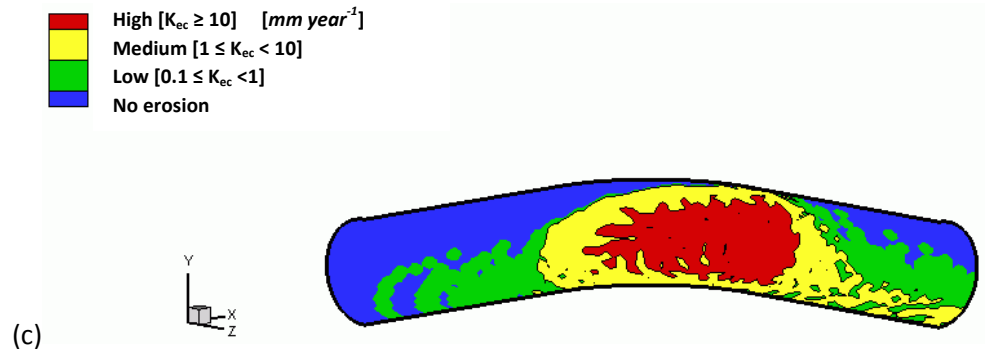

(c)

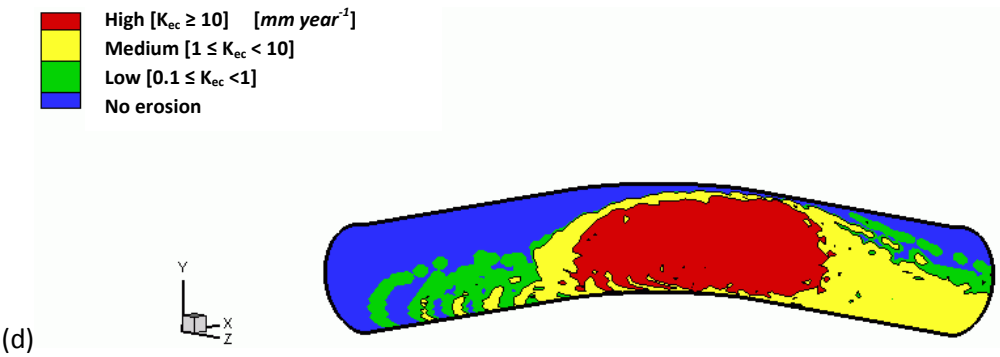

(d)

Figure 3: Erosion-corrosion wastage maps for the outer surface of elbow-pipe at pH=7, E_{AP} =-0.6 V[SCE], particle size=1000 [µm] and concentration =22.88% (vf= 0.1) for: (a) Fe. (b) Ni. (c) Cu. (d) Al.

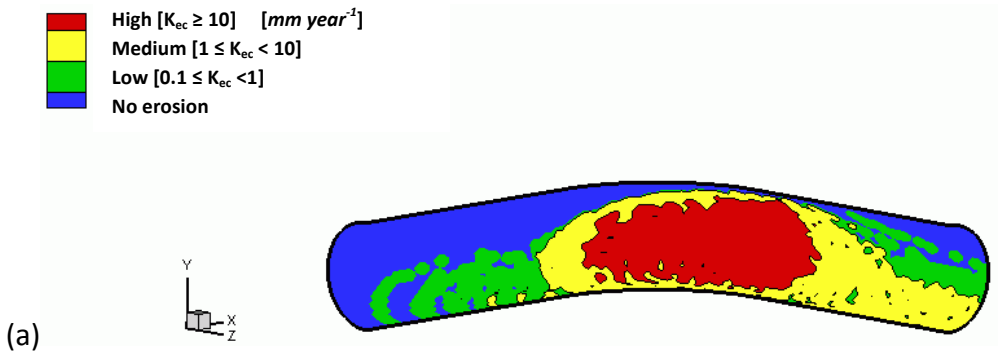

(a)

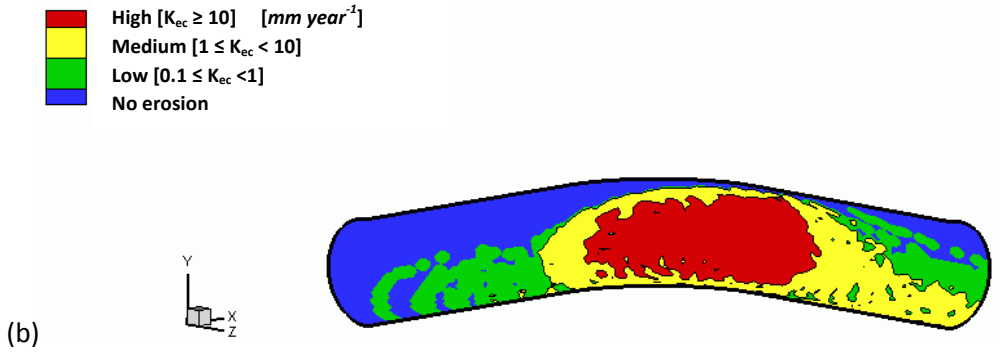

(b)

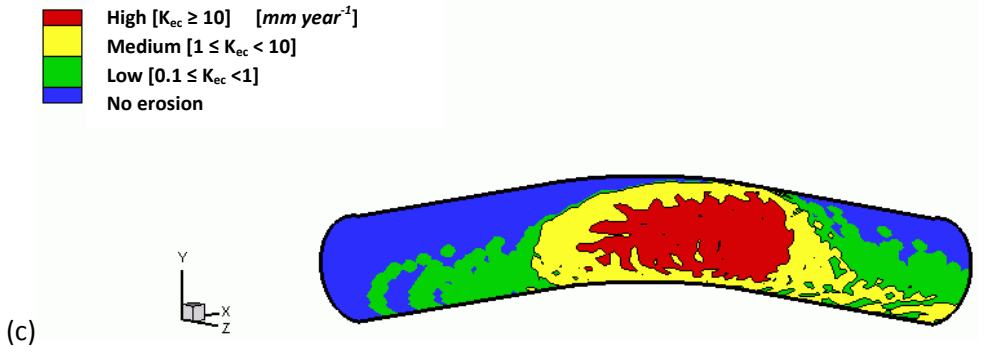

(c)

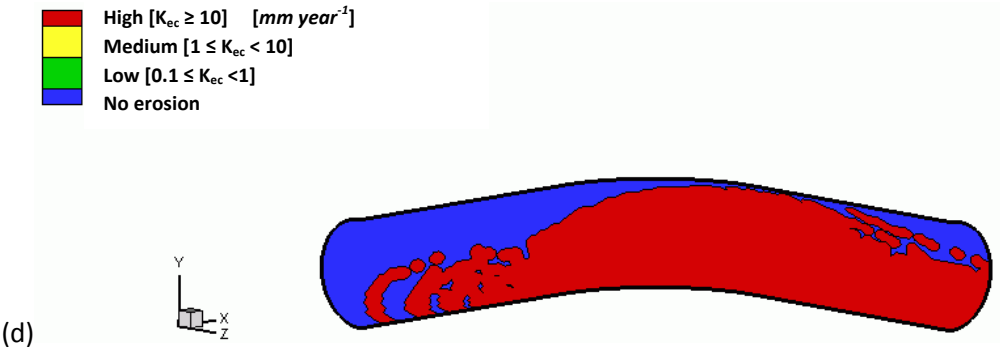

(d)

Figure 4: Erosion-corrosion wastage maps for the outer surface of elbow-pipe at pH=9, E_{AP} =-0.6 V[SCE], particle size=1000 [µm] and concentration =22.88% (vf= 0.1) for: (a) Fe. (b) Ni. (c) Cu. (d) Al.

Table 1: Properties for pure metals selected and their passive films

Metal Properties	Fe	Fe_2O_3	Ni	NiO	Cu	Cu_2O	Al	Al_2O_3	Silica particles
ρ [$kg\ m^{-3}$]	7800	5240	8900	6720	8930	6400	2700	3970	2670
k_2	1398.9	—	1571.7	—	1597.7	—	1058.5	—	—
E[*GPa*]	211		200		130		71	380	94
ν	0.293		0.312	T	0.343		0.345	0.22	0.3
H [*GPa*]	0.82	8.012	0.862	6.561	0.495	2.7362	0.260	20	—